Green Chemistry

Cutting-edge research for a greener sustainable future

rsc.li/greenchem

ROYAL SOCIETY
OF **CHEMISTRY**

PAPER
M. A. A. Mohamed, N. Gräßler *et al.*
Mechanochemical synthesis of Li-rich (Li$_2$Fe)SO cathode for
Li-ion batteries

PAPER

Mechanochemical synthesis of Li-rich (Li₂Fe)SO cathode for Li-ion batteries†

M. A. A. Mohamed, [ID] *[a,b] H. A. A. Saadallah,[a,b] I. G. Gonzalez-Martinez,[a] M. Hantusch,[a] M. Valldor, [ID] [c] B. Büchner, [ID] [a] S. Hampel [ID] [a] and N. Gräßler [ID] *[a]

Li-rich antiperovskite (Li₂Fe)SO with its high specific capacity is an attractive cathode material for Li-ion battery applications. While many battery materials depend on hazardous substances and their production is also rarely sustainable, we present an environmentally friendly and sustainable approach for the synthesis of Li-rich (Li₂Fe)SO using mechanochemistry based on ball milling. This one step process enables preparing a large quantity of phase-pure (Li₂Fe)SO using low-cost and non-toxic precursors, making it a viable alternative to current solid state synthetic method in terms of simplicity, laboratory safety and scalability. The obtained micro-sized particles are nearly spherical and have a small size distribution. To control the crystallinity and reduce the intrinsic defects of the ball-milled (Li₂Fe)SO material, a post-heat treatment procedure was tested. Thermodynamic measurements confirmed the high thermal stability of the ball-milled (Li₂Fe)SO material. Increasing the ball to powder weight ratio was found to be an effective strategy to decrease the milling time required for the synthesis, thus promoting energy saving. Overall, this work provides a practical guide for the green and scalable production of (Li₂Fe)SO cathode material, as well as a method for particle modification for improved electrochemical properties.

1. Introduction

The demand for Li-ion batteries (LIBs) in the market of portable electronics and electric vehicles is steadily growing due to their high energy density.[1–3] For the further development of LIBs, research is being conducted on cathode materials that combine low cost, sustainability and high performance.[1,3] Despite their great commercial success, current cathode materials such as LiCoO₂ (LCO), LiNi₁/₃Mn₁/₃Co₁/₃O₂, (NMC 111), LiNi₀.₈Co₀.₁₅Al₀.₀₅O₂ (NCA), LiMn₂O₄ (LMO) and LiFePO₄ (LFP) have specific limitations.[1,3] The recently reported (Li₂Fe)SO cathode, which belongs to the Li-rich antiperovskites with the general formula (Li₂TM)ChO (TM = Fe, Mn and Ch = S, Se), is a promising alternative with superior theoretical and practical specific capacities due to its multi-electron storage through cationic and anionic redox processes.[4–7] In addition, the antiperovskite (Li₂Fe)SO has low cost and toxicity compared to Co-containing cathode materials, which can reduce

the cost and environmental footprint of Li-ion batteries.[8–11] Numerous studies show approaches for recycling of Li-ion batteries including sulfur-containing materials as well.[12–14] The preparation of Li-rich (Li₂Fe)SO using non-toxic and low-cost raw materials such as lithium oxide, sulfur, and iron in a one-step solid-state reaction (SSR) has been reported.[4,5] This process is characterized by its simplicity and the absence of hazardous chemicals or solvents.[15] However, the solid-state method has two major disadvantages. The high temperature required for the reaction results in high energy consumption, and it is difficult to control the morphology and size distribution of the particles, which affect the electrochemical properties. Herein, we propose a new approach to prepare Li-rich (Li₂Fe)SO material using mechanochemistry (MC) by ball-milling (BM) to overcome the existing limitations in the SSR method.[16–18] In general, MC synthesis is recognized for its sustainability that can satisfy several points of the twelve principles of Green Chemistry.[19] In particular, the high laboratory safety, low production cost, high reproducibility, easily accessible and scalable equipment make it attractive for both laboratory and industrial applications.[19] We have monitored the mechanochemical synthesis of (Li₂Fe)SO by *ex situ* XRD measurements. It was found that several grams of phase-pure (Li₂Fe)SO, consisting of particles with primary micrometric size, can be obtained directly by ball milling. In contrast to the SSR method, the reaction is performed at room temperature, which is beneficial for energy saving and safety aspects. *Ex situ*

ᵃLeibniz Institute for Solid State and Materials Research (IFW) Dresden e.V., Helmholtzstraße 20, D-01069 Dresden, Germany. E-mail: n.graessler@ifw-dresden.de, m.a.a.mohamed@ifw-dresden.de
ᵇDepartment of Physics, Faculty of Science, Sohag University, 82524 Sohag, Egypt
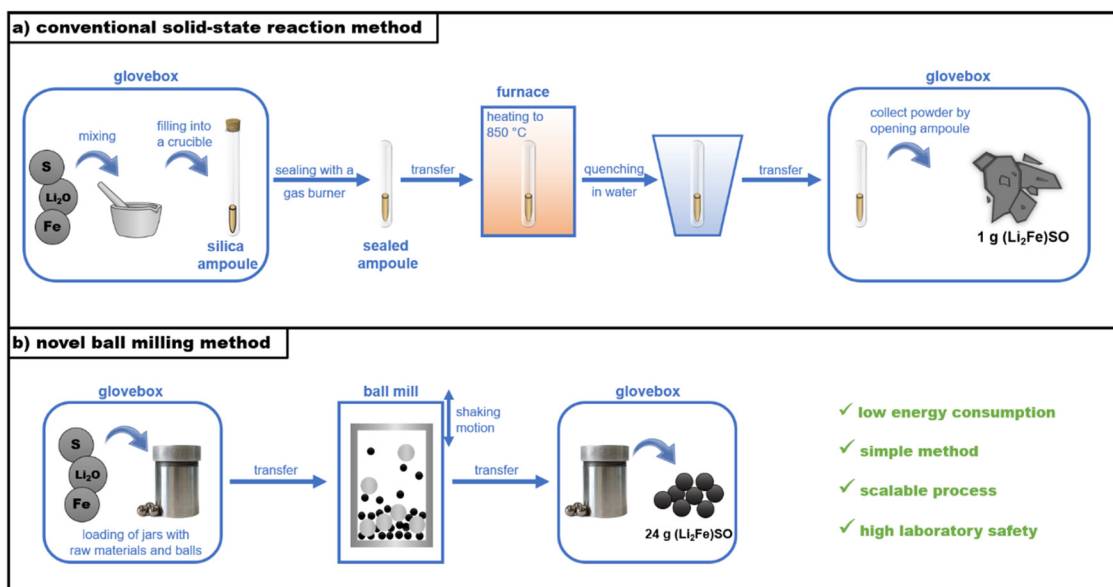ᶜDepartment of Chemistry, University of Oslo, Postbox 1033, Blindern, N - 0315 Oslo, Norway

Fig. 1 Schematic diagram of the synthesis procedures of (Li$_2$Fe)SO by the reported solid state reaction (a) and the novel mechanochemical (b) methods.

XRD measurements showed also low crystallinity of the ball-milled (Li$_2$Fe)SO sample, which comes from residual defects and amorphization caused by mechanical energy input.[15] To tune the structural and morphological properties of (Li$_2$Fe)SO cathode material, we investigated the effect of post-heat treatment as a guideline for improved electrochemical properties.

2. Results and discussion

2.1. One-step mechanochemical synthesis

Previously, the preparation of (Li$_2$Fe)SO was carried out *via* SSR method, requiring several steps as seen Fig. 1a.[5] In SSR method, the raw materials (Li$_2$O, Fe, and S) are mixed in an Ar-filled glove-box using an agate mortar and filled in a corundum crucible. The crucible is placed inside a silica tube which is temporarily closed by a rubber stopper. Afterwards, the silica tube is transferred outside the glovebox, evacuated, refilled with Ar gas to adjust the internal pressure to 200 mbar, and finally melt-sealed by a gas burner. The sealed ampoule is slowly heated up in a furnace (heating rate: 50 °C h^{-1}) to 750 °C and held at this temperature for 2–10 h. After the reaction, the ampoule is quenched in water which is necessary to prevent the formation of impurities. Finally, the silica ampule is inserted again in the glovebox and broken to extract the final product.

In contrast, MC synthesis of (Li$_2$Fe)SO involves the steps shown in Fig. 1b. The raw powders (Li$_2$O, Fe, and S) together with the stainless steels balls are loaded to the jar (milling reactor) inside the glovebox. Then, the closed jar is transferred to the milling machine and the reaction is performed. Eventually, the jar is opened inside the glovebox and the product is extracted. In MC synthesis, the mechanical energy due to collision events between balls and powder precursors results in continuous deformation, flattening, fracture and welding of the raw materials.[20,21] As a result, the nano-scaled composite material, formed from the selected constituents, contains defects, amorphous and/or metastable phases.[20] In the nano-scaled composite of powders, chemical reactions are induced across the grain boundaries of adjacent reactants due to local and temporary instants of mechanical friction.[20] These circumstances enhance the reaction kinetics by (i) reduction of the atoms diffusion length through formation of nanoscale grain size (ii) decreasing the reaction threshold energy induced by high residual energy in the form of structural defects (iii) continuous generation of fresh reactive surfaces by repeated fraction and welding of the raw materials.[20,21] As a result, MC approach can permit chemical reactions that normally happens at elevated temperature to be induced near-room temperature. There are a lot of variables that can influence the milling process such as the kind of the mill, the characteristics of the milling media (size, mass, mechanical strength and composition), milling media to sample ratio, filling degree of the milling chamber, milling atmosphere, milling speed, and milling time.[15] These parameters can change the nature of collision such as the stress frequency, stress energy and the quantity of trapped powder between the colliding particles, which eventually determine the amount of energy transfer.[15] The total amount of transferred energy (E_t) during milling process can be given as $E_t = SN \times \overline{SE}$, where SN is the number of stress events and $\overline{SE}$ is the average stress energy.[15] The average stress energy $\overline{SE}$ represents the maximum transferred energy to the reactants during a single collision and can be calculated as $\overline{SE} = \frac{V_R \times m_1 \times m_2}{2 \times (m_1 \times m_2)}$, where V_R and (m1 and m2) are the relative velocity and the masses of the colliding bodies, respectively.[15] The MC synthesis of

(Li$_2$Fe)SO offers significant advantages in various aspects compared to SSR as follows:

(i) Safety and environmental impact: MC reaction is performed in a tight stainless-steel chamber without usage of any external heating, which guarantees safe handling together with lower risk of explosion or gas release during the reaction compared to SSR method. Possible explosion of the silica tube used in SSR before completion of the reaction may be accompanied by release of volatile S gas (and possibly toxic H$_2$S because of a reaction with moist air at high reaction temperature) which is a risk on both the human health and environment. Besides, additional thermal quenching in water at high temperature (750 °C) is required to reduce the formed impurities during synthesis by SSR.[5] This sudden thermal perturbation exaggerates the risk of explosion.

(ii) Energy consumption: In this work, (Li$_2$Fe)SO is synthesised directly by MC without the need for any external thermal energy. This advantageous and not common feature allows controlling and reducing the consumed electrical energy by controlling the milling conditions such as the BPR or rotation velocity.[22] In contrast, SSR includes heating the sample to high temperature (750 °C) for long time with difficulty to optimize or reduce the consumed electrical energy.[5] Moreover, additional amount of energy is required in SSR to adjust the internal pressure by rotary pump.[5] It is worth mentioning that quantitative comparison of the consumed energy between MC (new approach) and reported SSR (highly optimized) approaches would not be fair due to (i) the different degree of optimizations, (ii) the different mass production (~1 g in SSR and ~24 g in MC), and (iii) the overestimation of the milling time by cooling of the reaction and relaxation of active amorphous phases during the here adopted step-by-step XRD protocol.

(iii) Monitoring of the reaction: The possibility of *in situ* and *ex situ* monitoring of the chemical reaction in MC method by several techniques gives opportunity to understand the intermediate chemical steps and mechanism.[19] These techniques can provide valuable information about potential overpressure inside the milling container and the volatile gases, which can be helpful in increasing the safety issue.[19] Although, *ex situ* technique is only applied here, our findings open the door for *in situ* investigations such as synchrotron X-ray diffraction, Raman spectroscopy, and real-time temperature sensing for more understanding of the reaction mechanism and better safety. In contrast, it is difficult to monitor the reaction in SSR method due to the used high temperature.

2.2. Monitoring of the mechanochemical reaction by *ex situ* XRD studies

The progress of the mechanochemical synthesis was monitored through periodic interruption of the grinding process, followed by extracting a small amount from the sample in the glovebox for XRD analysis, as shown in Fig. 2. The initial ball-to-powder weight ratio (BPR) was set at 3 : 1. After 8 hours of milling, XRD analysis revealed the presence of the diffraction peaks of (Li$_2$Fe)SO and some other secondary phases. These
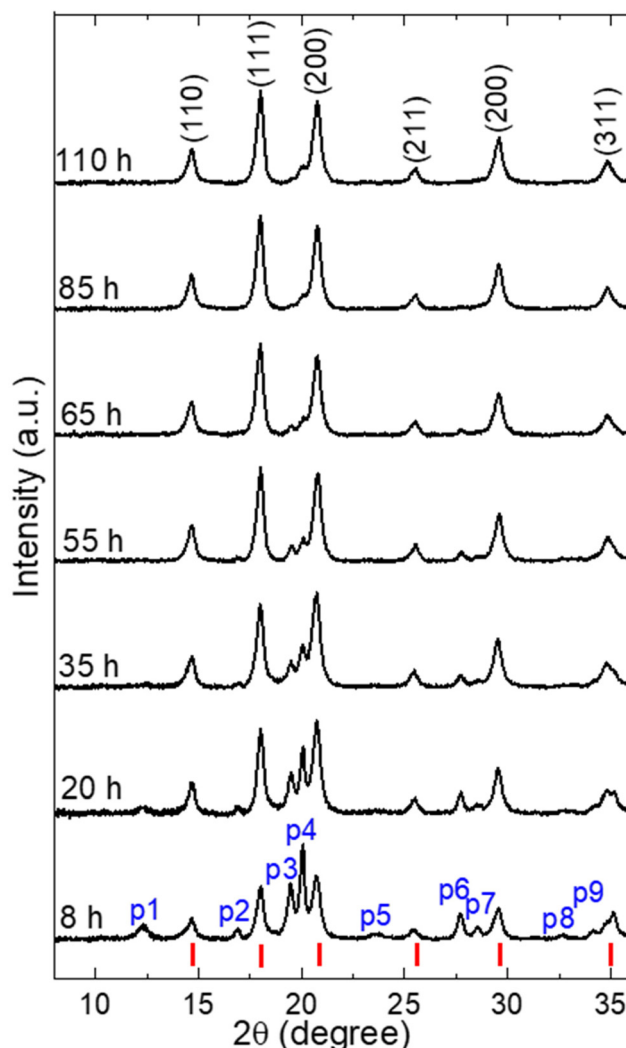

Fig. 2 XRD patterns of the milled powder as a function of the milling time using 3 : 1 as BPR. The labels (p1–p9) refer to the secondary phases, while the red marks (as reference) refer to the ideal Bragg positions of (Li$_2$Fe)SO.

secondary phases were labelled from p1 to p9, although some peaks remained unidentified due to the possibility of multiple phases existence at the same Bragg position (see Fig. S1†). With increasing the milling time, a progressive conversion to (Li$_2$Fe)SO phase takes place as indicated by the increase in the relative intensity of the (Li$_2$Fe)SO diffraction peaks. The improvement in the phase purity of (Li$_2$Fe)SO over time can be attributed to the increase in the energy transfer to the reactants.[15] Moving from 85 h to 110 h milling time, no noticeable change of the XRD pattern can be observed, which suggests a completion of the reaction. Nevertheless, a small peak (label p4) with a small shoulder is still visible. The minor secondary phase (p4) is determined as metallic iron (Fe) (1.2 vol%) by the Rietveld analyses (see Fig. S2†) which confirms the successful synthesis of almost pure (Li$_2$Fe)SO (space group: $Pm\bar{3}m$). The origin of this metallic Fe may come from either the unreacted

Fe from the raw powders, a slight contamination from the stainless-steel vial and/or balls, or a simultaneous contribution of both mentioned sources. Metallic Fe is electrochemically inactive and no significant effect of such a negligible amount on the electrochemical performance is expected. Despite applying such long milling time, (Li$_2$Fe)SO phase is still apparent, indicating its high mechanical stability. In the following discussions, it is referred to the sample obtained after 110 h as ball-milled (Li$_2$Fe)SO.

From the diffraction data a cubic lattice parameter for ball-milled (Li$_2$Fe)SO a = 3.935(5) Å is obtained, which is the comparable with the previously reported value (3.9139 Å).[5] By considering the peak broadening for the most intense diffraction peaks for the ball-milled (Li$_2$Fe)SO, the average crystallite size ($D_{Scherrer}$) was calculated from Debye Scherrer equation to be 9.98(8) nm.[23] In order to explore the effect of lattice strain contribution to the observed peak broadening, the average crystallite size ($D_{W–H}$) was recalculated again from Williamson–Hall (W–H) model (Fig. S3†).[24] W–H model yields $D_{W–H}$ of 12(1) nm comparable with $D_{Scherrer}$, which suggests minor contribution of the lattice strain to the peak broadening.

Interestingly, around 24 g is produced at the end of the milling, confirming the effectiveness of MC approach as a scalable technique. However, as expected by using dry milling, a minor amount of the powder (~3%) is stuck on the balls and the wall of the milling container which hinders complete removal of the powder.[25] Nevertheless, some studies confirm that the sticky powder can beneficially act as a protective layer to prevent the contamination from the milling medium and container.[26]

2.3. Effect of post-heat treatment

2.3.1. Crystallinity. The structural behavior of ball-milled (Li$_2$Fe)SO after post-heat treatment at different temperatures was investigated by XRD analysis (Fig. 3a). The results indicate that the crystallinity of the sample, as indicated by signal-to-noise ratio, does not show significant improvement until

temperature of 300 °C is reached. The trend of increasing crystallinity at higher temperatures is highlighted by the examples of the (111) and (200) peaks in Fig. 3b. Interestingly, the secondary phase p4 (metallic Fe) has disappeared at 300 °C, whereas p3 (as marked in Fig. 2) appeared again and increased in intensity until 400 °C and then decreased again at 500 °C (see Fig. 3a and b). To identify this secondary phase, Rietveld analyses for the ball-milled (Li$_2$Fe)SO followed by post-heat treatment at 500 °C was carried out as seen in Fig. S4.† The results confirmed the formation of (Li$_2$Fe)SO with simultaneous existence of minor secondary phases from FeS (0.15 vol%) and LiFeO$_2$ (0.2 vol%) corresponding to p3 peak. The disappearance of Fe upon heat treatment at 500 °C of the ball-milled (Li$_2$Fe)SO and appearance of FeS and LiFeO$_2$ may suggest a solid-state reaction between Fe and other minor amorphous species. However, the other probability of minor existence of FeS and LiFeO$_2$ in the ball-milled (Li$_2$Fe)SO and their appearance upon improvement of the crystallinity by heat treatment cannot be excluded. Although the electrochemical activity of LiFeO$_2$[27] and FeS,[28] their observed amounts in the heat-treated (at 500 °C) ball-milled (Li$_2$Fe)SO (0.15 vol%, and 0.2 vol%, respectively) suggest negligible contribution to the delivered capacity and the overall electrochemical performance. The decrease of XRD intensity of peak p3 at 500 °C suggests unstable thermal behaviour for its corresponding phases (FeS and LiFeO$_2$ based on Rietveld analysis).

The average crystallite size ($D_{Scherrer}$) and dislocation density (δ) of the heat-treated (Li$_2$Fe)SO samples were calculated and the results are shown in Fig. S5a.†[29] The $D_{Scherre}$ increases from 11.1(1) nm at 100 °C to reach its maximum value of 0.11(01) μm at 500 °C which agrees with expectation on thermal grain-size growth. In addition, the lattice parameter (Fig. S5b†) slightly decreases from 3.921(3) Å at 100 °C to reach 3.915 (3) Å at 500 °C which is very close to the ideal reported value (3.9139 Å).[5] This trend of the lattice parameter is attributed to strain relaxation and reduction of the internal structural defects such as lattice dislocations (as seen in
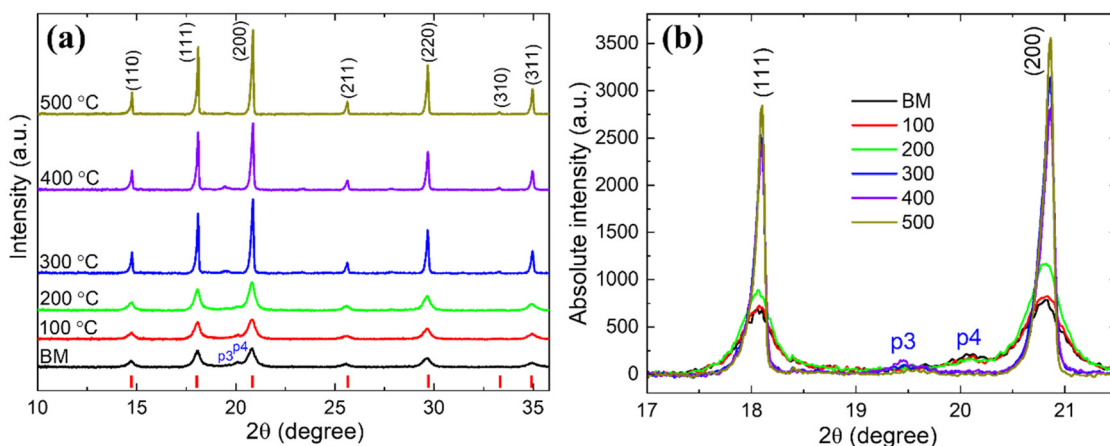

Fig. 3 Influence of the heat treatment temperature on the XRD of ball-milled (Li$_2$Fe)SO (BM) (a) and on the XRD intensity of (111) and (200) peaks (b). The red marks in (a) refer to the ideal Bragg positions of (Li$_2$Fe)SO as a reference.

Fig. S5a†), stacking faults, vacancies, and grain boundaries. Noteworthy, optimizing the internal lattice strain, which is feasible for (Li$_2$Fe)SO by post-heat treatment strategy, was recently reported to have strong influence on the electrochemical performance for other cathode materials.[30] This observation also confirms the possibility of using post-milling heat treatment to control the internal structure and crystallinity of (Li$_2$Fe)SO. Changing the material's crystallinity was reported to have a strong influence on the transport properties of Li$^+$ inside the material, with no general rule determining which has the higher ionic conductivity.[15]

2.3.2. Particle morphology. Fig. 4 displays the SEM images at low and high magnifications of ball-milled (Li$_2$Fe)SO (a, d) and ball-milled (Li$_2$Fe)SO followed by post-heat treatment at 300 °C (b, e) and 500 °C (c, f). As seen in Fig. 4a and d, the produced (Li$_2$Fe)SO by direct ball milling consists of irregular, nearly spherical dominantly micrometer-sized primary particles (<5 μm). The presence of some nano-sized flake-like structures is noteworthy (Fig. S6a†). These structures can be attributed to the flattening of the powder particles resulting from strong plastic deformation *via* high energy ball-milling.[21] Moreover, the agglomeration of these nanoflakes is due to the repeated cold-welding at low temperatures during the milling process (Fig. S6b†). As expected, the morphology of ball-milled (Li$_2$Fe)SO is completely different than its initial constituents (Li$_2$O, Fe and S) due to the effect of high mechanical energy on the morphology and particle size of the raw materials (Fig. S7†). Note, the crystallite size is different than particle size; the former estimates the crystalline domain size from the XRD peak broadening while the latter represents a physical dimension of a separate grain of the material and is obtained

from SEM.[31] The particle size of ball-milled (Li$_2$Fe)SO is larger than its crystallite size, indicating that each particle is composed of multiple crystallites. Compared to SSR method (Fig. S8†), MC synthesis produces much smaller particle size of (Li$_2$Fe)SO.[4] This reduction of the particle size can shorten the diffusion path length (*L*) for Li-ions, and thus, decreases the time constant for ionic diffusion (*t*) based on the relation $t = L^2/D$, where *D* is the solid-state chemical diffusion constant.[32] However, studying the effect of particle size on the electrochemical performance and kinetics of (Li$_2$Fe)SO is not the scope of this work. Subsequent heat treatment at 300 °C yields sintering of the tiny primary particles to form larger secondary particles (Fig. 4b and e). Further increase of temperature exaggerates the thermal sintering process and forms dominant secondary particles with much larger size compared to ball-milled (Li$_2$Fe)SO, as seen in Fig. 4c and f. Using post-heat treatment after ball milling, the size and shape of (Li$_2$Fe)SO particles can be carefully regulated. This requires striking a delicate balance between high crystallinity and the tendency of particles to agglomerate in order to minimize their surface energy.[33] The stoichiometry of the investigated samples was verified by energy dispersion spectroscopy (EDS) (Fig. S9 and Table S1†) and ICP-OES analysis (Table S2†) which confirmed the expected compositions.

TEM was used to further explore the effect of heat treatment on the internal structure and crystallinity of the ball-milled (Li$_2$Fe)SO. Fig. 5a–c reveal the HRTEM images at different magnifications of ball-milled (Li$_2$Fe)SO. Crystalline domains are clearly visible in Fig. 5b and c, highlighting the crystalline nature of the synthesized ball-milled (Li$_2$Fe)SO sample which is also supported by appearance of dotted rings (evidence of

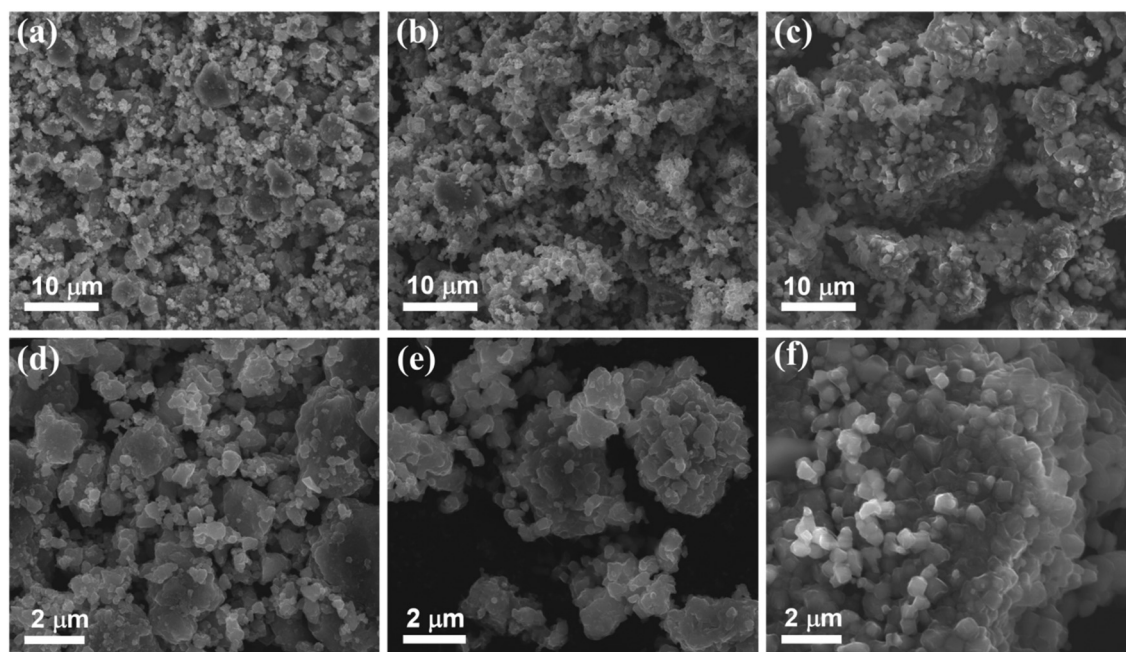**Fig. 4** SEM images at low and high magnifications for ball-milled (Li$_2$Fe)SO (a and d) and ball-milled (Li$_2$Fe)SO followed by post-heat treating at 300 °C (b and e) and 500 °C (c and f).
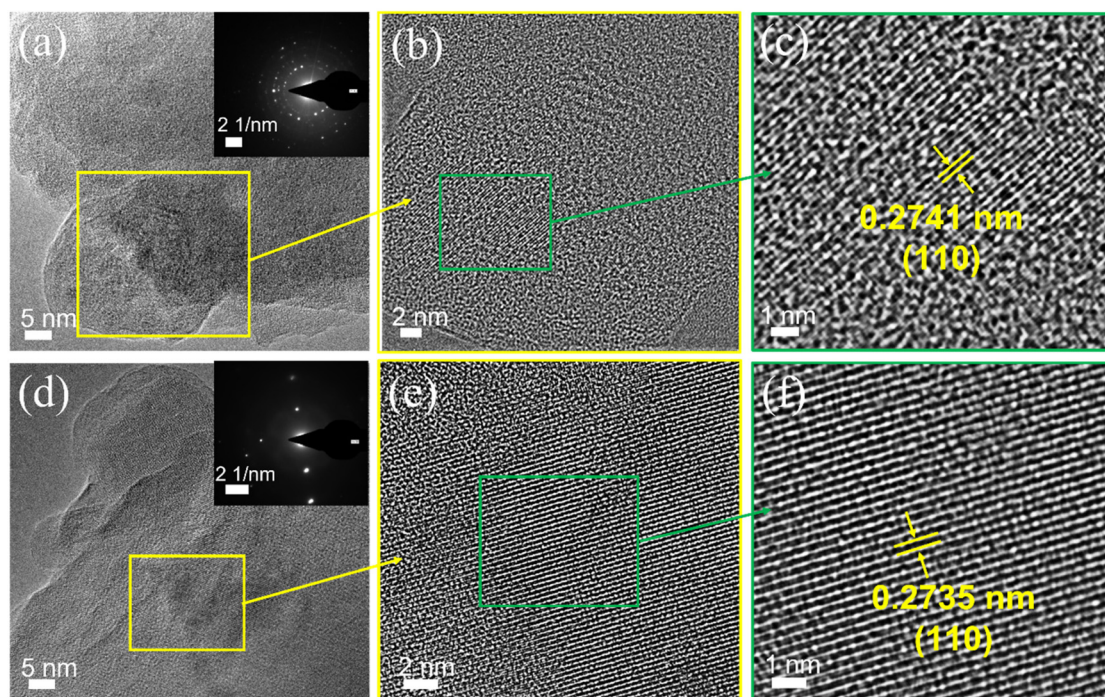
Fig. 5 TEM images for ball-milled (Li$_2$Fe)SO (a−c) and ball-milled (Li$_2$Fe)SO followed by post-heat treatment at 500 °C (d−f). The insets in Fig. 5a and d present the SEAD images.

Fig. 6 TEM image without (a) and with (b) marking the grain boundaries (yellow dashed lines) between the agglomerated grains/flakes of ball-milled (Li$_2$Fe)SO.

polycrystalline domains) in the selected area electron diffraction (SEAD) image (inset of Fig. 5a). Inverse Fourier transformation (FT) analysis and its corresponding plot profile (see Fig. S10a†) yield an average interplanar distance of ~0.2741 nm which in good agreement with *d* spacing for (110) plane of (Li$_2$Fe)SO. The appearance of flake-like nanostructures in Fig. 5 and 6 agree well with the SEM observation. The gradual change in color from black to gray, in Fig. 6b, indicates different thickness of the adjacent grains/flakes within the same particle due to cold welding effect.

Heat treatment of the ball-milled (Li$_2$Fe)SO at 500° C increases the crystallinity, as seen in Fig. 5e and f at different magnifications. This is confirmed by appearance of aligned

dots (evidence of single crystalline domain) in the SEAD data (inset of Fig. 5d) and further supported by increasing the crystalline domain size (Fig. 5e). Inverse FT and its corresponding plot profile (Fig. S10b†) produces an average interplanar distance of 0.2735 nm consistent with the (110) lattice plane of (Li$_2$Fe)SO. Interestingly, this value of lattice spacing is slightly lower than the value obtained for ball-milled (Li$_2$Fe)SO which is in good agreement with the XRD data (Fig. S5b†). A few crystalline domains with relatively high inter-planar spacing (~0.47 nm) are visible in the TEM image for the heat-treated (at 500 °C) ball-milled (Li$_2$Fe)SO (Fig. S11†), which coincides with the (101) lattice plane of hexagonal FeS.[34] This agrees well with Rietveld analysis (Fig. S4†) of existence of minor FeS impurity phase (0.15 vol%).

2.3.3. Thermodynamic properties. Fig. 7 illustrates the thermogram for the 1st and 2nd cycles of ball-milled (Li$_2$Fe)SO scanned in the temperature range from room temperature to 1100 °C. The thermal cycles display endothermal and exothermal peaks corresponding to the melting (~995.5 °C) and re-solidification (~974.5 °C) processes of the sample. These peaks were observed at similar temperatures in both cycles, which highlights the thermal reversibility and high purity of the synthesized ball-milled (Li$_2$Fe)SO. The absence of additional thermal processes besides melting and re-solidification confirms the stable behaviour of the sample under thermal treatment. Beside DTA, the ball-milled (Li$_2$Fe)SO was heated up to 1000 °C (higher than its melting temperature) and the corresponding XRD is shown in Fig. S12.† As seen, even after heat treatment at 1000 °C and cooling down
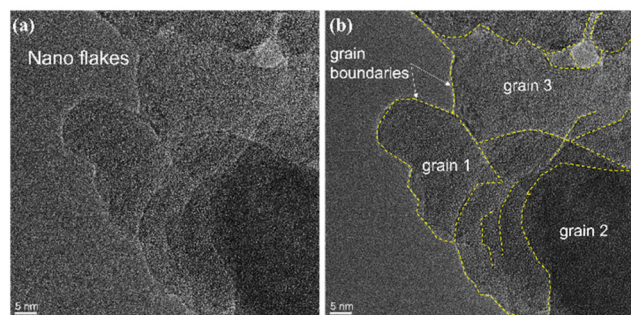
Fig. 7 DTA for ball-milled (Li$_2$Fe)SO.

upon heating at 1000 °C corresponding to a contraction of the unit cell. This behavior of unit cell contraction may be attributed to the strain relaxation and vanishing of the lattice defects. As a result of heat treatment at 1000 °C, the secondary phase p4 (metallic Fe) completely disappears while p3 (minor FeS and LiFeO$_2$) is still present. This indicates that the scenario described previously for the heat-treated (at 500 °C) ball-milled (Li$_2$Fe)SO sample is likely to occur. This highlights the good thermal stability of ball-milled (Li$_2$Fe)SO and agrees with the reported congruent melting, which is a unique advantageous feature for this class of cathode materials.[5] A similar thermal behavior is obtained for the (Li$_2$Fe)SO sample, that was heat-treated at 500 °C after milling with a slight increase of its melting point (Fig. S13†).

2.3.4. XPS studies. Fig. S14† compares the full X-ray photoelectron spectroscopy XPS survey spectra for (Li$_2$Fe)SO prepared by direct ball-milling and ball-milling followed by post-heat treatment at 500 °C. The overall spectrum confirms the existence of Li, Fe, S, and O elements in the sample surface. In addition, a slight appearance of carbon was verified by appearance of C 1s peak, which was used for charge correction calibrating (at ~285 eV). Fig. 8(a–d) compares the high-resolution spectra of Li 1s, Fe 2p, O 1s and S 2p for (Li$_2$Fe)SO prepared by direct ball-milling (BM) and ball-milling followed by post-heat
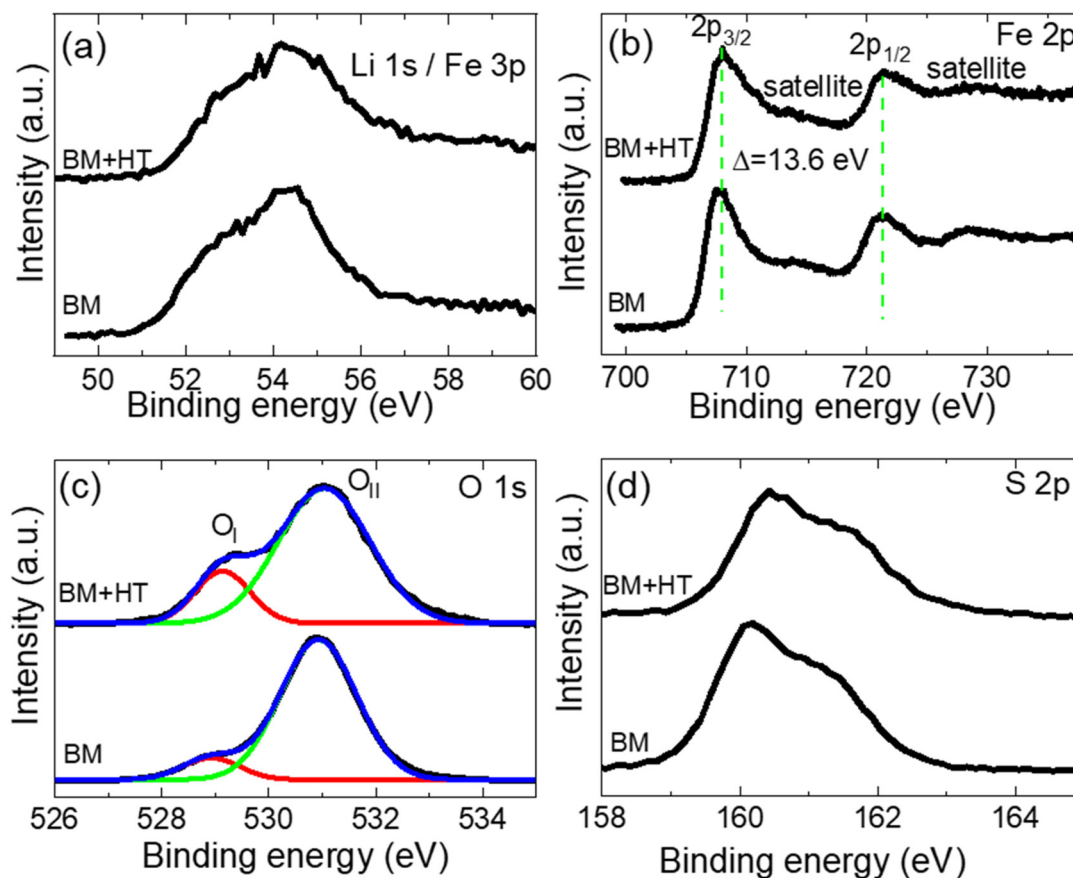
normally to room temperature, the (Li$_2$Fe)SO phase still exists. The XRD patterns in Fig. S12† show that by heating the sample above its melting point, the peaks for (Li$_2$Fe)SO phase increase in intensity and become sharper. Besides, a slight shift of all peak position to higher 2θ angles was observed

Fig. 8 XPS high-resolution spectrum of (a) Li 1s/Fe 3p, (b) Fe 2p, (c) O 1s, and (d) S 2p for (Li$_2$Fe)SO prepared by direct ball-milling (BM) and ball-milling followed by post-heat treatment at 500 °C (BM + HT).
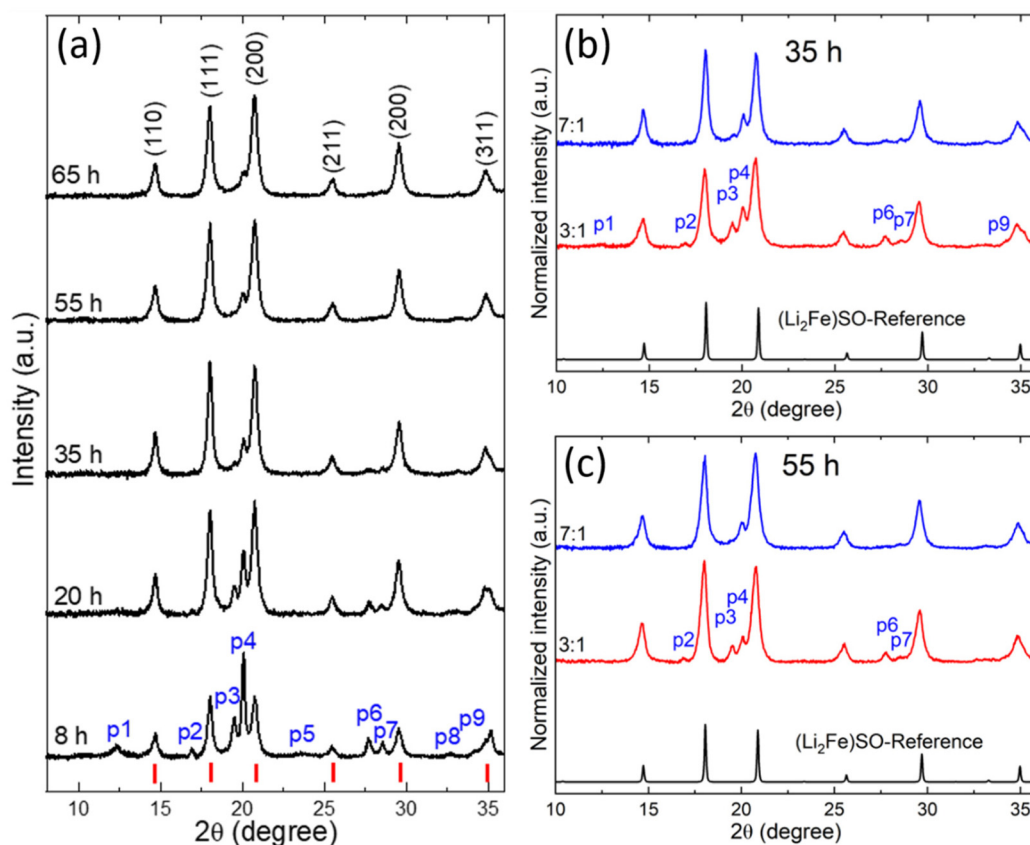
Fig. 9 XRD patterns of the milled powder as a function of the milling time using 7 : 1 as BPR (a) and comparison between different BPRs (3 : 1 and 7 : 1) at two milling times (b and c). The labels (p1–p9) refer to the secondary phases, while the red short lines in (a) represent the ideal Bragg positions for the (Li$_2$Fe)SO phase.

treatment at 500 °C (BM + HT). As shown in Fig. 8a, the high-resolution spectrum of Li 1s overlaps with Fe 3p, which makes it difficult to quantify the composition accurately, because the relative sensitivity factor of Fe 3p is higher 30 times than of Li 1s.[35] The Fe 2p for ball-milled (Li$_2$Fe)SO (Fig. 9b) is separated into two transitions (2p$_{1/2}$ and 2p$_{3/2}$) at different binding energies due to spin–orbit coupling.[35,36] Each transition is accompanied by appearance of a satellite feature at higher binding energy indicating the presence of Fe^{2+} in a high-spin state, as previously reported based on Mössbauer spectroscopy for (Li$_2$Fe)SO.[4] For ball-milled (Li$_2$Fe)SO as seen in Fig. 8b, the Fe 2p$_{1/2}$ and Fe 2p$_{3/2}$ appear approximately at 721.5 eV and 707.9 eV, agrees well with the values reported before for the same composition prepared by solid state reaction.[4] The O 1s high-resolution spectrum for the ball-milled (Li$_2$Fe)SO is deconvoluted into two parts as in Fig. 8c. The first part (O$_I$) appears at binding energy of ~529 eV while the second part (O$_{II}$) at ~531 eV. Part O$_I$ can be assigned to lattice oxygen, while the second part (O$_{II}$) is not precisely determinable. Previous study attributes the peak after the lattice oxygen (O$_{II}$ in this work) in the range 531–532 eV to oxygen vacancies.[37] However, recent report attributes that signal to the oxygen lattice with different coordination number adjacent to oxygen vacancies.[38]

On the other hand, other authors ascribed this signal to a contamination by chemisorbed oxygen species.[37] Fig. 8d presents S 2p peak for ball-milled (Li$_2$Fe)SO in the range 158.5–163.5 eV which consists of two overlapped parts (2p$_{1/2}$ and 2p$_{3/2}$) due to spin–orbit coupling. Overall, no significant change in the binding energies of (Li 1s/Fe 3p, Fe 2p, O 1s and S 2p peaks was observed upon subsequent heat treatment at 500 °C of the ball-milled (Li$_2$Fe)SO. However, an increase of the O$_I$ (lattice oxygen) contribution at the expense of O$_{II}$ is remarked upon heat treatment. This may be attributed to either a reduction of defects and enhancement of the lattice oxygen upon heat treatment or, most probably, decreasing of the chemisorbed oxygen species. Overall, the XPS studies indicate no change in the oxidation states of the constituent elements upon post-heat treatment after milling. This means that the crystallinity and morphology of ball-milled (Li$_2$Fe)SO can be easily controlled without affecting the electronic structure of the involved elements.

2.4. Optimization of the ball milling conditions

In section 2.1, we mentioned that different parameters affect the MC process such as a higher BPR. To verify this, we used a higher BPR (7 : 1 instead of 3 : 1) to increase the energy transfer and thus reduce the milling time, which further decreases the

energy consumption. The *ex situ* XRD patterns at different milling times using 7 : 1 BPR are shown in Fig. 9a. Note, BPR was controlled in this study by changing the number of balls while maintaining the same ball size. For comparison, the XRD of two selected milling times (35 h and 55 h) for the two samples milled with different BPR (3 : 1 and 7 : 1) are displayed in Fig. 9b and c, respectively. It is evident that at a given milling time, the increased BPR speeds up the conversion of the milled reactants into (Li$_2$Fe)SO phase. This comes from the improvement in the reaction kinetics by increasing the energy transfer.[22] Clearly, a similar XRD pattern to the ball-milled (Li$_2$Fe)SO (3 : 1 BPR and 110 h) was obtained after only 65 h milling time using 7 : 1 as BPR. This result confirms that the milling time used in producing (Li$_2$Fe)SO can be significantly reduced by increasing the BPR, which is a beneficial for energy saving. This also opens the way to further reduce the consumed energy by optimizing the milling parameters. The sustainable synthesis presented here, combined with the promising reported EC properties for antiperovskite (Li$_2$Fe)SO compared to other commercial cathodes (see Table S3†), pouches its progress as a potential cathode candidate.[4] Studying the effect of the synthesis conditions on the electrochemical performance of ball-milled (Li$_2$Fe)SO is planned for the future work.

3. Conclusions

We propose a facile, green, and scalable mechanochemical synthesis to prepare (Li$_2$Fe)SO cathode material. This novel approach can overcome the current obstacles of solid-state reaction method due to its simplicity, environmentally benign, and scalability. The *ex situ* XRD data confirms the successful preparation of (Li$_2$Fe)SO by direct mechanochemistry. The obtained nearly spherical particles are in the micrometer range with a small size distribution. Subsequent post-heat treatment strategy after ball-milling was found to be an effective strategy to control the internal structure, crystallinity, and morphology of the ball-milled (Li$_2$Fe)SO. Thermodynamic investigations confirmed the congruent melting with high thermal stability for the prepared samples. A strategy to significantly reduce the mechanochemical reaction time by increasing the ball-to-powder ratio was also introduced, which is beneficial for energy saving. Our findings highlight the advantages of mechanochemical synthesis in scaling up and controlling the structure and morphology of (Li$_2$Fe)SO cathode for tunable electrochemical properties.

4. Experimental details

4.1. Materials synthesis

Stoichiometric amounts of Li$_2$O, Fe and S powders (as bought from Alfa Aesar) were loaded into a stainless-steel jar in an argon-filled glovebox with controlled atmosphere (O$_2$ and H$_2$O < 1 ppm) from MBraun. The mixture was ball-milled using high energy SPEX SamplePrep 8000D with a rotation speed of 875 rpm at room temperature and using hardened stainless-steel balls with a size of 10 mm. Similar material (stainless steel) for grinding medium and milling container was chosen to prevent the contamination that might come from the abrasion and damage of the milling vial.[26] At the end of each milling process, the jar was opened inside the glovebox and the powder was extracted for further characterization. For the heat treatment of the samples after ball-milling, a certain amount of the sample was filled in a corundum crucible (Aliaxis, Frialit-Degussite, AL23) in glovebox. The crucible was placed into a silica tube (QSILAG; Quarzschmelze, Ilmenau) and temporarily closed with a rubber stopper. Outside the glovebox, the tube was evacuated to a pressure of less than 10^{-3} mbar, refilled with Ar to adjust the internal pressure to 0.2 bar, and sealed with a gas burner. The closed ampoule was placed into a furnace and heated at various temperatures (heating rate: 50 °C h^{-1}) for 3 h.

4.2. Characterization

4.2.1. X-ray diffraction (XRD). The prepared materials were analyzed by powder XRD (STOE STADI P diffractometer) using Debye–Scherrer mode with Mo K$_{\alpha 1}$ radiation source ($\lambda = 0.70926$ Å) and a Mythen 1 K detector (Dectris). The samples were filled into glass capillaries inside the glove box and finally melt-sealed to prevent any air exposure during XRD investigations. The average crystallite size ($D_{Scherrer}$) was calculated from Debye Scherrer equation $D_{Scherrer} = K\lambda/\beta \cos\theta$, where K is the shape factor (approximated to be 1), λ is the wavelength of the XRD source, β is the full width at half maximum obtained from Voigt fitting of the XRD peaks and subtracting the instrumental broadening, and θ is the Bragg angle.[23] The dislocation density (δ), which indicates the number of defects in the sample, was calculated using the formula $\delta = 1/(D_{Scherrer})$.[29]

4.2.2. Elemental analysis. Inductively coupled plasma-optical emission spectroscopy (ICP-OES) (iCAP 6500 Duo View, Fa. Thermo Fisher Scientific GmbH) was used to estimate the stoichiometry of the produced compositions in terms of molar ratios of the elements.

4.2.3. Morphology investigations. Scanning electron microscopy (Nova-NanoSEM 200) coupled with energy dispersive spectroscopy (EDS Genesis with 15 kV accelerating voltage) was used to evaluate the morphology and composition of the studied compounds.

4.2.4. Thermal analysis. Differential thermal analysis (DTA) up to 1200 °C was performed by a Setaram DTA92-2400 (alumina container) under helium atmosphere (heating rate: 10 °C min^{-1}).

4.2.5. Transmission electron microscopy (TEM). High resolution transmission Electron Microscopy (HR-TEM) studies were performed using a FEI Titan 80–300, equipped with a Cs corrector, and operated at 300 kV. The sample was loaded by direct contact onto Cu 300 mesh TEM grids (Agar) and holey carbon film. The Fourier transformation analyses were carried out by ImageJ software.

4.2.6. X-ray photoelectron spectroscopy (XPS).
X-ray photoelectron spectroscopy (XPS) was performed with a PHI 5600 spectrometer (Physical Electronics) using monochromatic Al-Kα radiation (250 W) equipped with a hemispherical analyzer with 29.35 eV pass energy for high resolution spectra. To prevent any air exposure, the sample was transferred in a special transfer chamber. The estimated spot size on the sample is about 0.4 mm. To avoid charging effects, an electron gun was used as a neutralizer for each measurement.

Conflicts of interest

There are no conflicts to declare.

Acknowledgements

References

1 A. Manthiram, *Nat. Commun.*, 2020, **11**, 1–9.

2 D. Deng, *Energy Sci. Eng.*, 2015, **3**, 385–418.

3 N. Nitta, F. Wu, J. T. Lee and G. Yushin, *Mater. Today*, 2015, **18**, 252–264.

4 D. Mikhailova, L. Giebeler, S. Maletti, S. Oswald, A. Sarapulova, S. Indris, Z. Hu, J. Bednarcik and M. Valldor, *ACS Appl. Energy Mater.*, 2018, **1**, 6593–6599.

5 K. T. Lai, I. Antonyshyn, Y. Prots and M. Valldor, *J. Am. Chem. Soc.*, 2017, **139**, 9645–9649.

6 M. A. A. Mohamed, M. V. Gorbunov, M. Valldor, S. Hampel, N. Gräßler and D. Mikhailova, *J. Mater. Chem. A*, 2021, **9**, 23095–23105.

7 M. A. A. Mohamed, L. Singer, H. Hahn, D. Djendjur, A. Özkara and E. Thauer, *J. Power Sources*, 2023, **558**, 232547.

8 B. E. Murdock, K. E. Toghill and N. Tapia-Ruiz, *Adv. Energy Mater.*, 2021, **11**, 2102028.

9 A. Butt, G. Ali, K. Tul Kubra, R. Sharif, A. Salman, M. Bashir and S. Jamil, *Energy Technol.*, 2022, **10**, 2100775.

10 H. Munir, R. R. Srivastava, H. Kim, S. Ilyas, M. K. Khosa and B. Yameen, *J. Chem. Technol. Biotechnol.*, 2020, **95**, 2286–2294.

11 S. Ilyas, R. Ranjan Srivastava, V. K. Singh, R. Chi and H. Kim, *Waste Manage.*, 2022, **154**, 175–186.

12 L. Schwich and B. Friedrich, *Metals*, 2022, **12**, 1108.

13 L. Schwich, P. Sabarny and B. Friedrich, *Metals*, 2020, **10**, 1513.

14 Y. Li, W. Lv, H. Huang, W. Yan, X. Li, P. Ning, H. Cao and Z. Sun, *Green Chem.*, 2021, **23**, 6139–6171.

15 A. Banik, T. Famprikis, M. Ghidiu, S. Ohno, M. A. Kraft and W. G. Zeier, *Chem. Sci.*, 2021, **12**, 6238–6263.

16 A. Perona, P. Hoyos, Á. Farrán and M. J. Hernáiz, *Green Chem.*, 2020, **22**, 5559–5583.

17 J. Andersen and J. Mack, *Green Chem.*, 2018, **20**, 1435–1443.

18 J. L. Do and T. Friščić, *ACS Cent. Sci.*, 2017, **3**, 13–19.

19 K. J. Ardila-Fierro and J. G. Hernández, *ChemSusChem*, 2021, **14**, 1–19.

20 T. Tsuzuki, *Commun. Chem.*, 2021, **4**, 143.

21 P. F. M. De Oliveira, R. M. Torresi, F. Emmerling and P. H. C. Camargo, *J. Mater. Chem. A*, 2020, **8**, 16114–16141.

22 J. Jepsen, G. Capurso, J. Puszkiel, N. Busch, T. Werner, C. Milanese, A. Girella, J. B. von Colbe, M. Dornheim and T. Klassen, *Metals*, 2019, **9**, 349.

23 Y. Y. Kim, A. S. Schenk, J. Ihli, A. N. Kulak, N. B. J. Hetherington, C. C. Tang, W. W. Schmahl, E. Griesshaber, G. Hyett and F. C. Meldrum, *Nat. Commun.*, 2014, **5**, 4341.

24 P. Muhammed Shafi and A. Chandra Bose, *AIP Adv.*, 2015, **5**, 057137.

25 C. Liu, M. Wu, Y. Liu, Z. Lu, Y. Yang, S. Shi and G. Yang, *Mater. Res. Bull.*, 2018, **99**, 436–443.

26 I. Lahiri and K. Balasubramanian, *Bull. Mater. Sci.*, 2007, **30**, 157–161.

27 Y. Hu, X. Liu and N. Tapia-Ruiz, *J. Mater. Sci.*, 2020, **55**, 8651–8664.

28 C. Li, A. Sarapulova, K. Pfeifer and S. Dsoke, *ChemSusChem*, 2020, **13**, 986–995.

29 M. Dongol, A. El-Denglawey, M. S. Abd El Sadek and I. S. Yahia, *Optik*, 2015, **126**, 1352–1357.

30 S. S. Kim, D. N. Agyeman-Budu, J. J. Zak, A. Dawson, Q. Yan, M. Cában-Acevedo, K. M. Wiaderek, A. A. Yakovenko, Y. Yao, A. Irshad, S. R. Narayan, J. Luo, J. Nelson Weker, S. H. Tolbert and K. A. See, *Chem. Mater.*, 2022, **34**, 3236–3245.

31 W. Xie, E. Polikarpov, J. Choi, M. E. Bowden, K. Sun and J. Cui, *J. Alloys Compd.*, 2016, **680**, 1–5.

32 J. Zhang, J. Qiao, K. Sun and Z. Wang, *Particuology*, 2022, **61**, 18–29.

33 M. Ullah, M. E. Ali and S. B. A. Hamid, *Rev. Adv. Mater. Sci.*, 2014, **37**, 1–14.

34 X. Wang, Q. Xiang, B. Liu, L. Wang, T. Luo, D. Chen and G. Shen, *Sci. Rep.*, 2013, **3**, 1–8.

35 R. Dedryvère, M. Maccario, L. Croguennec, F. Le Cras, C. Delmas and D. Gonbeau, *Chem. Mater.*, 2008, **20**, 7164–7170.

36 A. P. Grosvenor, B. A. Kobe, M. C. Biesinger and N. S. McIntyre, *Surf. Interface Anal.*, 2004, **36**, 1564–1574.

37 J. C. Dupin, D. Gonbeau, P. Vinatier and A. Levasseur, *Phys. Chem. Chem. Phys.*, 2000, **2**, 1319–1324.

38 H. Idriss, *Surf. Sci.*, 2021, **712**, 2–7.